Eddy-induced meridional transport variability at ocean western boundary

Xiaoming Zhai[a,*], Zhibin Yang[b]

[a] *Centre for Ocean and Atmospheric Sciences, School of Environmental Sciences, University of East Anglia, Norwich, UK*

[b] *Key Laboratory of Physical Oceanography and Frontiers Science Center for Deep Ocean Multispheres and Earth System, Ocean University of China, Qingdao, China*

Abstract

Meridional transport variability induced by westward-propagating eddies impinging on the western boundary is investigated both analytically and numerically. A simple theory is first developed in the framework of the reduced-gravity model which relates eddy-induced meridional transport to eddy thickness anomalies propagated into the western boundary by long Rossby waves, and this is followed by a suite of numerical model experiments. It is found that eddies impinging on the western boundary excite boundary waves that propagate equatorward along the western boundary, which leads to coherent meridional overturning circulation (MOC) anomalies equatorward of the incident eddy field. The magnitude and duration of eddy-induced MOC anomalies are variable and irregular, ranging from less than 1 Sv to over 5 Sv and from less than 10 days to over 100 days. Importantly, these eddy-induced MOC anomalies lead to considerable meridional heat transport variability across the latitudes, with implications for seasonal and interannual climate

*Corresponding author

Email address: `xiaoming.zhai@uea.ac.uk` (Xiaoming Zhai)

variability and prediction.

Keywords: Ocean eddy, Meridional overturning circulation, Western boundary, Ocean modelling

1. Introduction

The meridional overturning circulation (MOC) of the global ocean dominates the exchange of water as well as climatically-important properties it carries between ocean basins and across latitudes within the basins. For example, in the subtropical North Atlantic, the MOC transports approximately 1 PW (1 PW = 10^{15} W) of heat northward, with important consequences for European climate and Arctic sea-ice variability (e.g. Vellinga and Wood, 2002; Mahajan et al., 2011).

As revealed by recent RAPID array observations (e.g. Cunningham et al., 2007; McCarthy et al., 2012), the strength of the MOC varies on all time scales. On decadal and longer time scales, the MOC variability is found to be closely related to low-frequency changes of basin-wide wind stress field and high-latitude surface buoyancy flux (e.g. Eden and Willebrand, 2001; Cessi and Louazel, 2001; Johnson and Marshall, 2002; Zhai et al., 2014). On the shorter seasonal and interannual time scales, the MOC variability is often attributed to higher frequency wind-driven Ekman transport fluctuations (e.g. Jayne and Marotzke, 2001; Biastoch et al., 2008). This understanding of MOC variability, which is based primarily on linear theory and coarse-resolution ocean model simulations, is linear and deterministic in nature, that is, any changes of the MOC can be traced back to changes in external forcing.

On the other hand, the ocean is populated with nonlinear mesoscale eddies which dominate the ocean's kinetic energy spectra (e.g. Ferrari and Wunsch, 2009; Chelton et al., 2011; Ni et al., 2020). Apart from in the Antarctic Circumpolar Current and separated western boundary currents, these nonlinear eddies are observed to propagate ubiquitously westward (Chelton et al., 2011; Ni et al., 2020). Upon arriving at the western boundary, the majority of the energy associated with the eddies is dissipated within the narrow western boundary region due to processes such as loss of balance (Zhai et al., 2010; Yang et al., 2021). While the eddy energy is shown to be dissipated at the western boundary, the fate of volume anomalies carried westward by the eddies is much less clear. It is possible that pressure anomalies are built up by eddies impinging on the western boundary, which subsequently drive anomalous alongshore boundary current transport.

There have been extensive studies of the dynamics of a large, isolated eddy interacting with a side boundary (e.g. Smith and O'Brien, 1983; Smith, 1986; Shi and Nof, 1994; Sutyrin et al., 2003; Frolov et al., 2004; Wei and Wang, 2009). For example, Shi and Nof (1994) showed that when an eddy encounters a sidewall it migrates in the alongshore direction under the influence of the beta force, image effect and "rocket" effect and they found that the image effect usually dominates. With the addition of a continental shelf and slope, the eddy-boundary interaction becomes more complicated; it results in the spinup of secondary cyclones/anticyclones and the excitation of topography waves (e.g. Sutyrin et al., 2003; Frolov et al., 2004; Wei and Wang, 2009). However, the focus of these studies has been primarily on the evolution and trajectory of an incident eddy upon its arrival at a side boundary.

To our knowledge, there have been few studies investigating the eddy-induced meridional transport and MOC variability. Thomas and Zhai (2013) isolated the contribution of eddies to MOC variability in an eddy-permitting model of the North Atlantic by forcing it with climatological and steady surface forcing. They found that the eddy-induced MOC variability is ubiquitous and significant at all latitudes, with a magnitude comparable to the seasonally forced MOC, particularly in the subtropics. Furthermore, the eddy-induced MOC variability is found to manifest not only at high frequencies (e.g. days to weeks) but also at seasonal and longer time scales. Marshall et al. (2013) proposed that the Stokes drift or bolus transport associated with westward propagating Rossby waves and eddies is returned eastward through Eulerian-mean currents, which they termed Rossby rip currents. More recently, Domingues et al. (2019) investigated the impact of eddy-like westward-propagating signals on the Florida Current variability using controlled realistic numerical experiments, and they found both a direct response involving eddy-wall interaction and an indirect response involving eddy perturbation of Gulf Stream meandering. Although these realistic modelling studies have highlighted the potential significance of eddy-induced MOC variability, a theoretical understanding and analysis is still lacking.

In this study, we investigate meridional transport variability induced by westward-propagating eddies impinging on the western boundary using a combination of linear theory and idealised model simulations. The paper is organised as follows. In section 2, a simple theory is developed in the framework of a reduced-gravity model which relates eddy-induced meridional transport to eddy thickness anomalies propagated into the western boundary by long Rossby waves. In section 3, results from a suite of numerical model experiments are presented, ranging from a simple Gaussian eddy interacting with vertical western sidewall to satellite-derived ocean eddy field interacting with realistic western boundary geometry. Finally, the key findings from this study are summarised and discussed in section 4.

2. Eddy-induced western boundary transport

Following the earlier theoretical work of Godfrey (1975) and Minobe et al. (2017), here we consider the volume budget of a narrow western boundary layer in the Northern Hemisphere (enclosed by the dotted lines in Fig. 1) and derive eddy-induced meridional transport in the framework of a reduced-gravity model. We start with the linear continuity equation

$$\frac{\partial h}{\partial t} + H\left(\frac{\partial u}{\partial x} + \frac{\partial v}{\partial y}\right) = 0, \tag{1}$$

where u and v are the zonal and meridional velocities, and h is the upper layer thickness anomaly from its initial value H.

Integrating (1) from the western boundary at $x = x_w$ to just outside the western boundary layer at $x = x_b$, while noting the no-normal-flow boundary condition at the western boundary, i.e. $u = 0$ at $x = x_w$, we get

$$\int_{x_w}^{x_b} \frac{\partial h}{\partial t}\, dx + u_b H + \frac{\partial T}{\partial y} = 0, \tag{2}$$

where $u_b(y,t)$ is the zonal velocity anomaly at $x = x_b$, associated with the incident eddy field, and $T(y,t) = \int_{x_w}^{x_b} vH dx$ is the meridional alongshore boundary current transport.

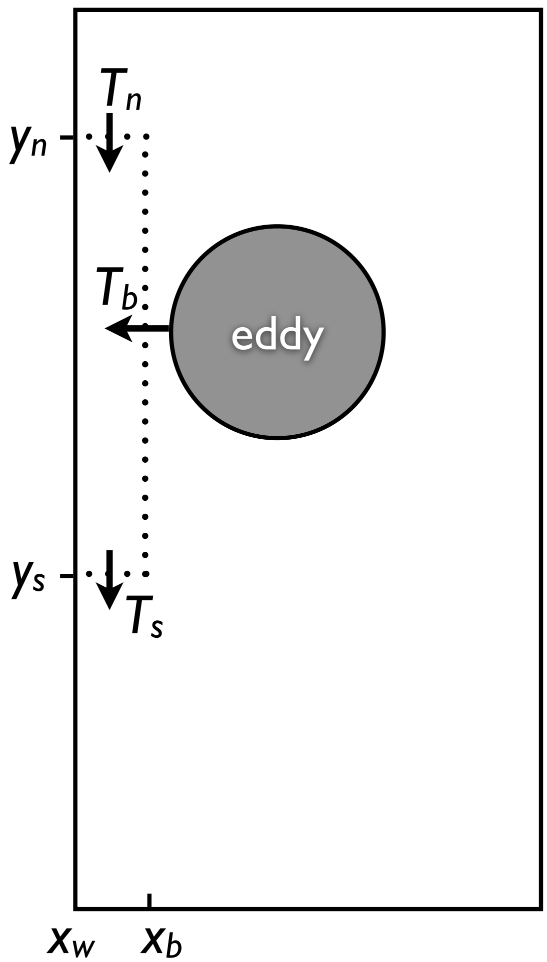

Figure 1: Schematic of volume budget for a narrow western boundary layer enclosed by the dotted lines, where T_b is eddy volume flux into the western boundary by long Rossby waves integrated over the latitude range of the incident eddy field, and T_n and T_s are meridional western boundary current transports at y_n and y_s respectively.

Outside of the western boundary layer, the geostrophic balance applies, i.e.,

$$f u_b = -g' \frac{\partial h_b}{\partial y}, \tag{3}$$

where $f(y)$ is the Coriolis parameter, g' is the reduced gravity, and $h_b(y,t)$ is the upper layer thickness anomaly at $x = x_b$.

Now substituting (3) into (2) and integrating between latitudes at the northern (y_n) and southern (y_s) limits of the incident eddy field (Fig. 1), we obtain the volume budget for the narrow western boundary layer

$$\int_A \frac{\partial h}{\partial t}\, dA - \int_{y_s}^{y_n} c(y) h_b \, dy + T_n - T_s = 0. \tag{4}$$

Here A is the horizontal area of the western boundary layer, T_n and T_s are meridional western boundary current transports at y_n and y_s respectively, and $c(y) = \beta g' H / f^2$ is the long Rossby wave speed, where $\beta = df/dy$ is the meridional gradient of the Coriolis parameter. In deriving (4), integration by parts is used and h_b is assumed to vanish at $y = y_n$ and $y = y_s$. Physically, (4) states that the volume change in the western boundary layer is caused by eddy thickness anomalies propagating into the western boundary layer from the ocean interior at long Rossby wave speeds as well as the difference between meridional alongshore boundary transports at the two bounding latitudes of the eddy field.

Anomalies arriving at the western boundary excite boundary trapped waves that propagate equatorward and thereby set up T_s. In the absence of forcing further to the north of the eddy field, $T_n = 0$. For large eddies approaching a narrow western boundary layer where the zonal scale of the eddies is much greater than the western boundary width, the time lag caused by eddy thickness anomalies crossing the narrow western boundary layer can be neglected. Furthermore, for time scales of interest to this study, i.e., longer than the boundary wave adjustment time, the time derivative term in (4) is small (Minobe et al., 2017). In this case, (4) simplifies to

$$T_s(t) \approx -\int_{y_s}^{y_n} c(y) h_b \, dy = -\int_{y_s}^{y_n} \frac{\beta g' H}{f^2} h_b \, dy. \tag{5}$$

Eq. (5) shows that the eddy-induced western boundary transport at latitudes immediately equatorward of the incident eddy field depends on eddy thickness anomalies propagated into the western boundary by long Rossby waves integrated over the latitude range of the whole eddy field. Furthermore, the amplitude of this eddy-induced boundary transport remains constant equatorward of $y = y_s$ because of the absence of westward propagation of eddy thickness anomalies equatorward of the eddy field. The dependence of T_s on long Rossby wave speeds shown in (5) further indicates that, for eddies with the same h_b, those at lower latitudes are capable of generating greater transport variability at the western boundary. Note that the alongshore eddy migration owing to the sidewall image effect can potentially delay the leakage of eddy thickness anomalies via boundary wave propagation and thereby introduce additional lag between the time eddy thickness anomalies crossing $x = x_b$ and the time they crossing $y = y_s$. On the other hand, the presence of a realistic continental shelf often does not allow the eddies to come close enough to the western boundary to permit a significant interaction with their images (e.g. Sutyrin et al., 2003; Frolov et al., 2004). For example, experiments of Sutyrin et al. (2003) demonstrated that the centre of an eddy needs to be within a distance of less than its radius to the western wall for the image effect to come into play.

With Eq. (5), one can further infer sea level anomalies induced by the incident eddies at the western boundary. The alongshore flow in the western boundary layer is approximately in geostrophic balance, i.e.,

$$fv = g' \frac{\partial h}{\partial x}. \tag{6}$$

Zonally-integrating (6) across the western boundary layer at $y = y_s$ while noting that $h_b = 0$ at $y = y_s$, we obtain another equation for T_s,

$$T_s = -\frac{g'H}{f_s} h_w, \tag{7}$$

where h_w is the upper layer thickness anomaly at $x = x_w$ and $y = y_s$.

Combining (5) and (7), a solution for layer thickness anomaly at the western boundary immediately equatorward of the incident eddy field is obtained

$$h_w(t) = f_s \int_{y_s}^{y_n} \frac{\beta}{f^2} h_b(y,t)\, dy. \tag{8}$$

In the reduced-gravity model, the sea level and upper ocean thickness anomalies are related via $g\eta = g'h$. As such, the sea level anomaly at the western boundary, $\eta_w(t)$, depends on eddy sea level anomalies just outside of the western boundary layer, $\eta_b(y,t)$, in a similar way, i.e.,

$$\eta_w(t) = f_s \int_{y_s}^{y_n} \frac{\beta}{f^2} \eta_b(y,t)\, dy. \tag{9}$$

A similar relationship between sea level at the western boundary and sea level at the western end of the ocean interior was also derived by Godfrey (1975) and Zhai et al. (2014) for a meridional western boundary and by Minobe et al. (2017) for a curved western boundary, both with vertical sidewalls. For a more general solution of $\eta_w(t)$ that accounts for contribution of western boundary sea level anomalies further to the north of y_n, readers are referred to Minobe et al. (2017). Eq. (7) shows that due to the f_s factor the amplitudes of layer thickness and sea level anomalies at the western boundary decay toward the equator equatorward of the incident eddy field. This can be understood as follows: constant alongshore transport equatorward of the eddy field (see Eq. (5)) requires smaller cross-shore pressure difference at lower latitudes, as dictated by geostrophy (Marshall and Johnson, 2013). Note that the presence of a continental shelf and slope can attenuate the influence of the interior sea level on sea level at the coast, especially if the continental shelf and slope are wide and bottom friction is small (Wise et al., 2018). However, the focus of these previous studies is primarily on boundary sea level anomalies generated by large-scale wind and thermohaline forcing in the open ocean, and there have been few theoretical studies on meridional transport variability at the western boundary induced by an incident mesoscale eddy field.

2.1. A single Gaussian eddy

We first consider the case of an idealised Gaussian-shaped eddy immediately outside of a narrow western boundary layer in the Northern Hemisphere, with the centre of the eddy initially located at $(x_b + R,\, y_0)$ where R is the e-folding radius of the eddy. The eddy is then assumed to propagate westward at the long Rossby wave speed of c_0. As a result, the eddy centre moves westward according to $x = x_b + R - c_0 t$, and the layer thickness anomaly associated with the eddy is given by

$$h(x, y, t) = Ae^{-\frac{[x-(x_b+R-c_0 t)]^2+(y-y_0)^2}{R^2}}, \tag{10}$$

where A is the eddy amplitude. We obtain the evolution of layer thickness anomaly at $x = x_b$ by letting $x = x_b$ in (10),

$$h_b(y,t) = Ae^{-\frac{(c_0 t - R)^2}{R^2}} e^{-\frac{(y-y_0)^2}{R^2}}. \tag{11}$$

Substituting (11) into (5), we then obtain meridional transport at the western boundary induced by this Gaussian eddy, i.e.,

$$T_s(t) \approx -A\sqrt{\pi} R c_0 e^{-\frac{(c_0 t - R)^2}{R^2}}. \tag{12}$$

Assuming that the Gaussian eddy is anticyclonic with an amplitude of $A =$ 200 m, a radius of $R = 100$ km and a westward-propagating speed of $c_0 = 2$ cm s^{-1}, the amplitude of T_s increases and then decreases with time, with a peak value of about -0.7 Sv (negative means southward; 1 Sv = 10^6 m^3 s^{-1}) at $t = R/c_0$.

2.2. Random eddies

When there is a chain of Gaussian-shaped eddies that are initially lined up meridionally and immediately outside of the western boundary layer in the latitude band between y_s and y_n, the eddy-induced western boundary transport at $y = y_s$ (and also equatorward of y_s) is given by

$$T_s(t) = -\sqrt{\pi} \sum_{i=1}^{N} A_i R_i c_i e^{-\frac{(c_i t - R_i)^2}{R_i^2}}, \tag{13}$$

where N is the total number of eddies between y_s and y_n, and A_i, R_i and c_i are the amplitude, radius and propagating speed of the i-th eddy, respectively. Eq. (13) shows that the eddy-induced transport variability at the western boundary equatorward of incident eddies depends on eddy anomalies arriving at the western boundary integrated over the whole eddy field, with larger, stronger eddies and those at lower latitudes making a greater contribution. In situations where eddies of the same polarity arrive simultaneously at the western boundary, they are able to generate particularly large meridional transport anomalies. Note that (13) assumes that eddies propagate westward at long Rossby wave speeds and neglects random eddy movement owing to eddy-eddy interaction.

3. Numerical model experiments

We now conduct a suite of numerical experiments using the MIT general circulation model (MITgcm; Marshall et al., 1997), ranging from a simple Gaussian eddy interacting with vertical western sidewall to satellite-derived ocean eddy field interacting with realistic western boundary geometry, to examine eddy-induced meridional transport variability.

3.1. Idealised eddy field

The model simulations are first initialised with either a single Gaussian eddy or a sea of random eddies. The model domain is a rectangular basin that is 16.6 degrees in zonal extent (35 degrees for the case of random eddies), 80 degrees in meridional extent (90 degrees for random eddies), and 4 km deep with vertical sidewalls and a flat bottom. The horizontal grid spacing is chosen to be $1/12^\circ \times 1/12^\circ$ to permit a vigorous mesoscale eddy field. There are 70 geopotential levels whose thicknesses increase with depth, ranging from 5 m at the surface to 165 m close to the bottom. We employ a linear equation of state that depends only on temperature and a quadratic bottom friction with a drag coefficient of 2×10^{-3}. Sponges are applied at the northernmost

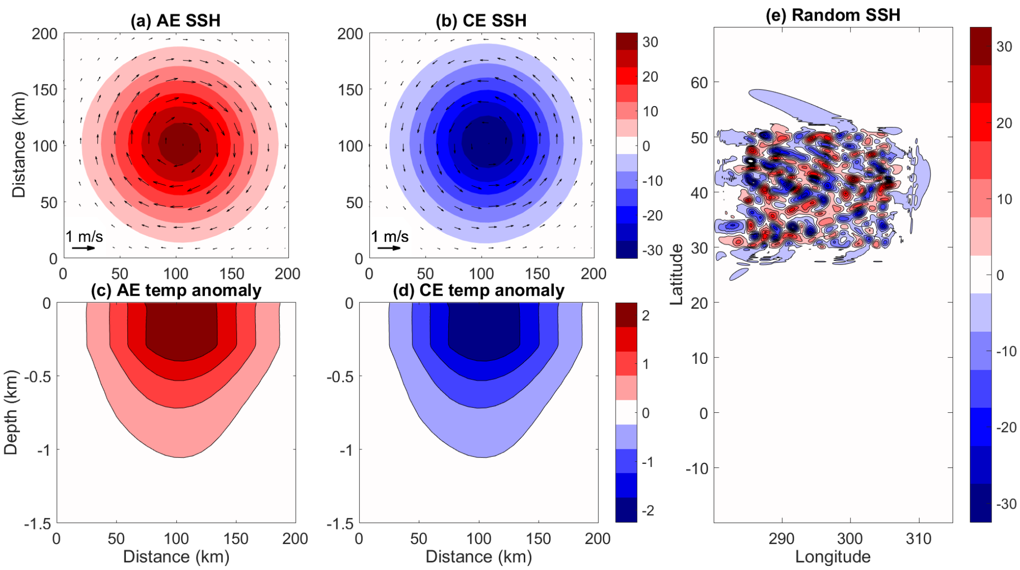

Figure 2: SSH (cm) fields on day 1 in experiments initialized with (a) a single AE, (b) a single CE and (e) a sea of random eddies. Arrows represent eddy geostrophic velocities. (c) and (d) show vertical transects of initial eddy temperature anomalies (°C) in AE and CE experiments, respectively.

and southernmost 10 degrees of the model domain to damp waves excited by eddy-western boundary interaction approaching these boundaries.

For the single eddy experiments, we initialise the model with a surface-intensified Gaussian-shaped mesoscale eddy that is in thermal wind balance:

$$T'(x,y,z) = \begin{cases} T'_s G(x,y), & \text{if } z > \delta \\ T'_s G(x,y) \exp\left(-\frac{5}{2}\frac{z-\delta}{D-\delta}\right), & \text{if } z < \delta \end{cases}$$

where z is the vertical coordinate positive upward, $T'(x,y,z)$ is the temperature anomaly associated with the eddy, $T'_s = 2.5$°C is the maximum eddy temperature anomaly at the surface, $G(x,y) = \exp\left(-\frac{5}{2}\frac{(x-x_0)^2+(y-y_0)^2}{R^2}\right)$ is the horizontal Gaussian function, $\delta = 300$ m is the depth of the upper layer, $R = 100$ km is the eddy radius, and $D = 1500$ m is the eddy depth range. The eddy thermal structure used in this study is similar to that in Vic et al. (2015), but with some minor modifications to ensure a smooth transition at $z = \delta$. The background vertical stratification is derived from the climatological temperature field of the U.S. Navy's Generalised Digital Environmental Model (GDEM). Assuming that the horizontal eddy velocities vanish at the bottom, we integrate the equation of hydrostatic balance over the water column to deduce the eddy pressure field, and from that we obtain the horizontal eddy velocities at each depth via geostrophic balance. Figure 2a-d shows the initial eddy temperature and velocity fields used in the single anticyclonic eddy (AE) experiment and single cyclonic eddy (CE) experiment. Both the AE and CE experiments run for 200 days.

Following Zhai et al. (2010) and Yang et al. (2021), we then conduct another two model experiments (Random and Random2 hereafter), with each initialised with a sea of random eddies (Fig. 2e). In these two experiments, the initial eddy sea surface height (SSH) field is constructed via a superposition of zonal and meridional Fourier modes (Brannigan et al., 2015; Ni et al., 2020):

$$\eta = \eta_0 \sum_{k,l=1}^{8} \sin\left(2\pi kx + \phi_1\left(k,l\right)\right) \sin\left(2\pi ly + \phi_2\left(k,l\right)\right),$$

where $\eta_0 = 25$ cm is the maximum eddy SSH amplitude, k and l are the zonal and meridional wavenumbers respectively, and ϕ_1 and ϕ_2 are random phases. For the initial eddy temperature field, we make use of the vertical eddy temperature profile obtained from composite analysis of satellite altimetry and Argo float data in the northwest Atlantic region (Zhang et al., 2013). Since this composite vertical temperature profile is normalised by the eddy

SSH anomaly, we combine it with the initial eddy SSH field to generate the initial 3D eddy temperature. Finally, the initial eddy horizontal velocity is derived from a combination of eddy SSH and temperature anomalies via geostrophic balance (see also Yang et al., 2021), similar to the single eddy experiments. Due to the wider model domain, Random and Random2 are run for a longer period of time, that is, 500 days.

3.2. Satellite-derived eddy field

As a step towards more realistic simulations, we conduct an additional ensemble of twelve experiments in a regional Atlantic model (Atlantic hereafter) that are initialised with realistic bathymetry and satellite-derived SSH anomalies. The regional Atlantic model domain spans the area between 260°W and 18.9°E and between 20°S and 60°N. There are 50 geopotential levels whose thicknesses increase with depth, ranging from 10 m at the surface to 456 m close to the bottom. Instead of vertical sidewalls and flat bottom, realistic topography from the General Bathymetric Chart of the Oceans (GEBCO) is used in the Atlantic ensemble experiments. The other model parameters remain the same as in Random. The daily gridded global SSH anomaly data produced and distributed by the Copernicus Marine Environment Monitoring Service are interpolated from its $0.25° \times 0.25°$ grid onto the $1/12° \times 1/12°$ Atlantic model grid before they are combined in the same way as in Random with the normalised vertical eddy temperature profile from the Argo-composite analysis to generate the initial 3D eddy temperature and horizontal velocity fields.

We conduct an ensemble of twelve experiments by initialising the regional Atlantic model with satellite-derived SSH anomalies on twelve different days,

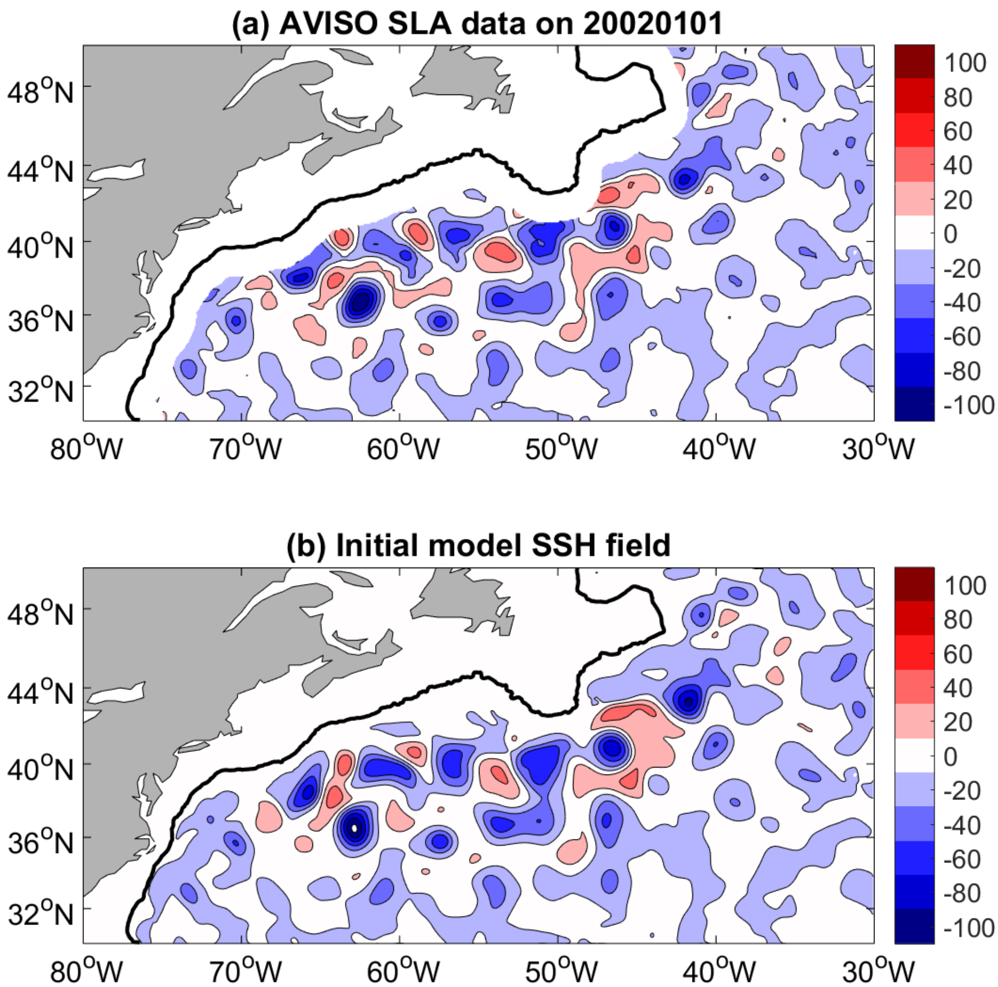

Figure 3: (a) Satellite-derived SSH anomaly field (cm) on January 1st, 2002. Note that SSH anomalies within1.5 degrees to the east of 2000-m isobath (black lines) are removed. (b) SSH field (cm) in one of the Atlantic experiments after the model has been integrated forward for 20 days with model temperature strongly restored towards the initial 3D eddy temperature field.

that is, the first days of Januaries and Julies in year 2002-2005 and the first days of Aprils and Octobers in year 2002-2003. Since the aim of this study is to examine meridional transport variability induced by eddies impinging on the western boundary, we exclude in the model initial conditions SSH anomalies that are within 1.5 degrees to the east of the 2000-m isobath (Fig. 3a). Each ensemble member is integrated forward for 20 days with the truncated SSH field and with model temperature strongly restored towards the initial 3D eddy temperature field. In this way, the initially-truncated SSH field to the east of the 2000-m isobath is allowed to evolve into closed SSH contours (Fig. 3b) and the eddy velocity field further adjusts to the eddy temperature and SSH fields to reduce mismatch. After this initial 20-day adjustment, each ensemble experiment is run for 300 days.

4. Results

4.1. Single eddy experiments

The AE and CE in the single eddy experiments propagate westward at speeds close to the phase speeds of long Rossby waves, with the AE drifting slightly equatorward and the CE drifting slightly poleward (Fig. 4a), as often found in satellite observations (e.g. Chelton et al., 2007; Ni et al., 2020). Upon encountering the vertical sidewall at the western boundary, the AE and CE generally migrate equatorward and poleward, respectively, owing to the image effect of the sidewall (e.g. Shi and Nof, 1994). The amplitudes of both eddies, defined as maximum/minimum SSH for AE/CE, decay with time due to frictional energy dissipation in the western boundary eddy "graveyard" (Fig. 4b; Zhai et al., 2010; Yang et al., 2021).

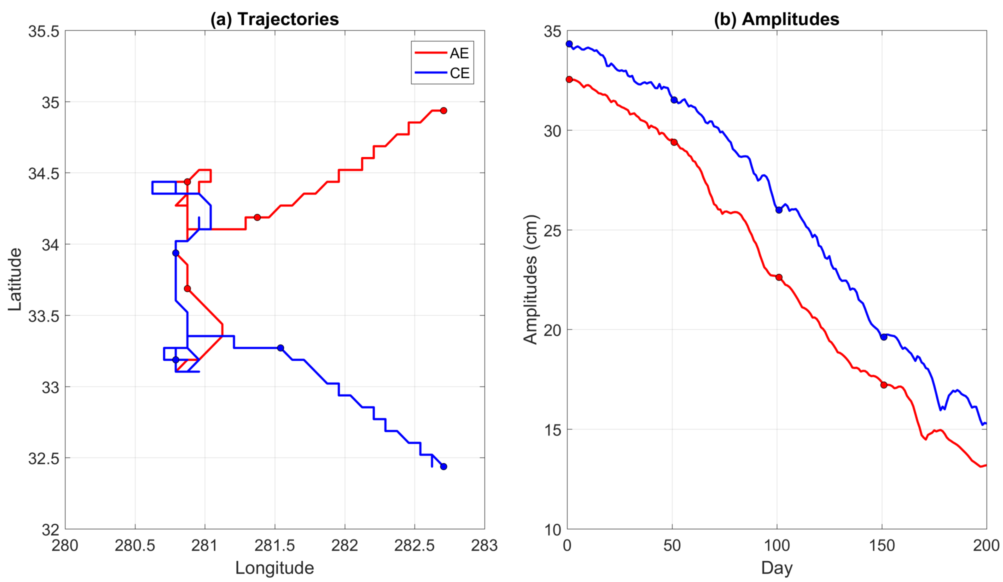

Figure 4: Eddy (a) trajectories and (b) amplitudes (cm) in AE (red) and CE (blue) experiments. The blue and red dots in (a) and (b) indicate eddy locations and amplitudes every 50 days.

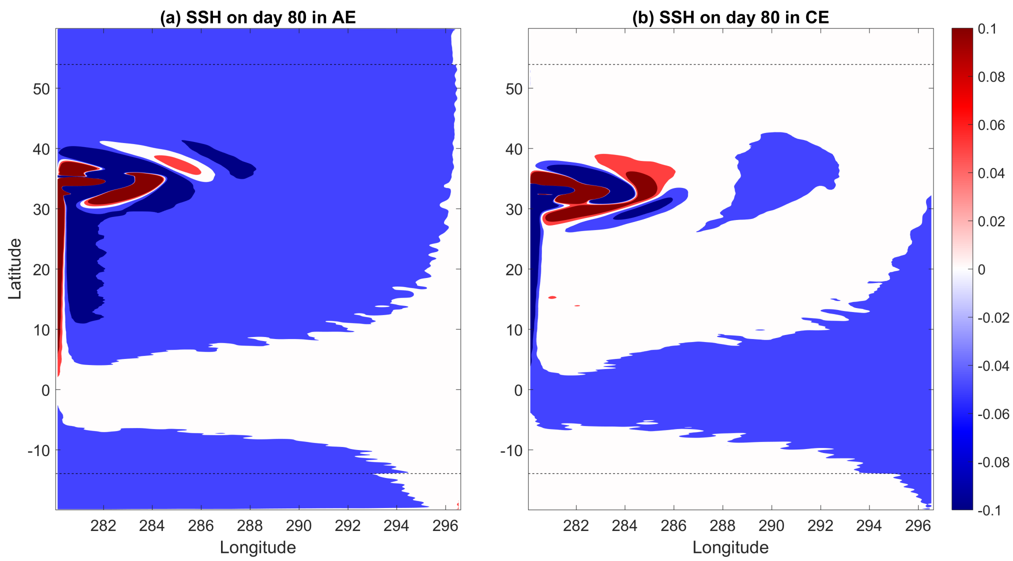

Figure 5: SSH (cm) fields on day 80 in (a) AE and (b) CE experiments. The dashed black lines mark the boundaries of the sponge layers. Note that the colour scale is heavily saturated to reveal regions of moderate SSH anomalies.

Figure 5 shows the model SSH fields on day 80 in the single eddy experiments, shortly after the arrival of the eddy centres at the western boundary. The eddy-sidewall interaction excites short Rossby waves and generates smaller satellite eddies, which leads to a complex SSH pattern at the eddy incident latitudes. To the south of the eddy incident latitudes, a simpler picture emerges. The positive (negative) SSH anomaly associated with the AE (CE) is seen to leak equatorward along the western boundary, eastward along the equator, and then poleward along the eastern boundary, followed by the slow radiation of Rossby waves into the ocean interior, in a manner similar to the ocean response to large-scale wind and thermohaline forcing (e.g. Johnson and Marshall, 2002; Zhai et al., 2014). This boundary wave adjustment process is likely the reason behind the coherent MOC structure induced by eddies at latitudes south of the Gulf Stream found in the realistic Atlantic model of Thomas and Zhai (2013).

Given the meridional coherence of eddy-induced MOC south of the eddy incident latitudes, we plot the time series of the MOC streamfunction at the 20°N latitude in the single eddy experiments (Fig. 6). The MOC streamfunction is the integral of zonally-integrated meridional transport from the surface to a given depth, and is defined as $V(y,z,t) = \int_{x_w}^{x_e} \int_z^0 v(x,y,z,t)\, dz\, dx$, where $x = x_e$ is the model eastern boundary and z is the depth. As the AE arrives at the western boundary, it generates positive SSH and upper ocean pressure anomalies at the western boundary, setting up zonal pressure difference across the western boundary region (and also across the model domain), which, via geostrophy, drives southward upper ocean meridional transport and negative MOC anomalies. These pressure and MOC anomalies propagate equator-

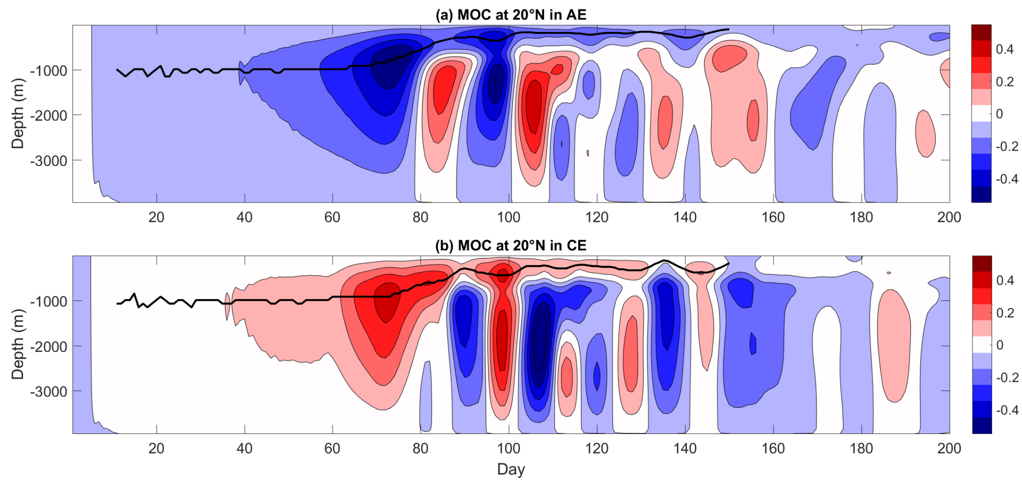

Figure 6: Eddy-induced MOC (Sv) at 20°N in (a) AE and (b) CE experiments. The contour interval is 0.1 Sv. Black lines indicate the depth of upper ocean MOC anomalies used in the comparison between theory and model simulation shown in Fig. 7a.

ward along the western boundary and arrive at 20°N on about day 40 (Fig. 6). The negative MOC anomaly then intensifies and reaches its maxmixum strength of ∼0.5 Sv on day 70 before it weakens and switches sign at depths below ∼1000 m on day 80. Over the rest of the simulation period, the MOC anomaly at 20°N remains negative in the upper 500-800 m, while below that it displays overturning cells of alternating signs and short durations. These short-duration deep cells are most likely associated with the smaller eddies generated during the AE-western wall interaction (e.g. Sutyrin et al., 2003; Frolov et al., 2004; Wei and Wang, 2009), a process that is not accounted for in our simple theory. We therefore focus on comparison between the theory and MOC anomalies in the upper ocean of the model (black lines in Fig. 6).

For meridional transport at 20°N, (5) can be re-written, after substituting

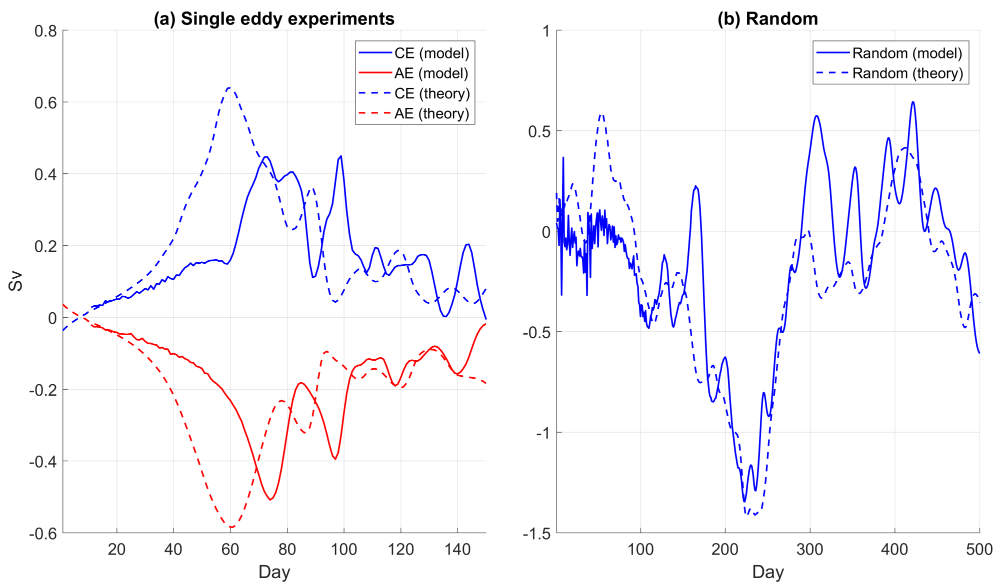

Figure 7: Comparison between theoretically-predicted (dashed) and model-simulated (solid) MOC anomalies at 20°N in (a) the single eddy experiments and (b) Random.

$g\eta_b = g'h_b$, as

$$T_{20\mathrm{N}}(t) = -\int_{20\mathrm{N}}^{50\mathrm{N}} \frac{\beta g H}{f^2} \eta_b \, dy. \tag{14}$$

In (14), the integral is limited to 50°N since northward of 50°N is the model sponge layer. We then estimate MOC anomalies at 20°N using (14) with $H = 600$ m inferred from the initial eddy structure and η_b (SSH anomalies 80 km to the east of the western sidewall) from model output. Time series of MOC predicted by our simple theory compares reasonably well with that simulated by the model, albeit the modelled MOC lags the theoretically-predicted MOC by about 15 days (Fig. 7a). We attribute this time lag to the time it takes for the eddy to cross the narrow western boundary region as well as the sidewall image effect, both of which are neglected in the theory (see Section 2).

4.2. Random

In experiments initialised with a sea of random eddies, the eddies propagate westward while at the same time interact with each other and cascade energy towards larger scales. Upon encountering the western sidewall, the eddies again generate pressure anomalies that propagate equatorward along the western boundary in the form of coastal trapped Kelvin waves, resulting in meridionally coherent MOC anomalies to the south of the incident eddy latitude band (30-50°N). Figure 8 shows the time series of MOC streamfunctions at 20°N as well as meridional heat transport across this latitude in Random and Random2. The meridional heat transport is defined as $\mathcal{H}(y,t) = \int_{x_w}^{x_e} \int_{-H_b}^{0} \rho_0 c_p v(x,y,z,t) T(x,y,z,t) \, dz \, dx$, where $\rho_0 = 1027.5$ kg m^{-3} is the reference density, $c_p = 4200$ J kg^{-1} °C^{-1} is the specific heat of sea

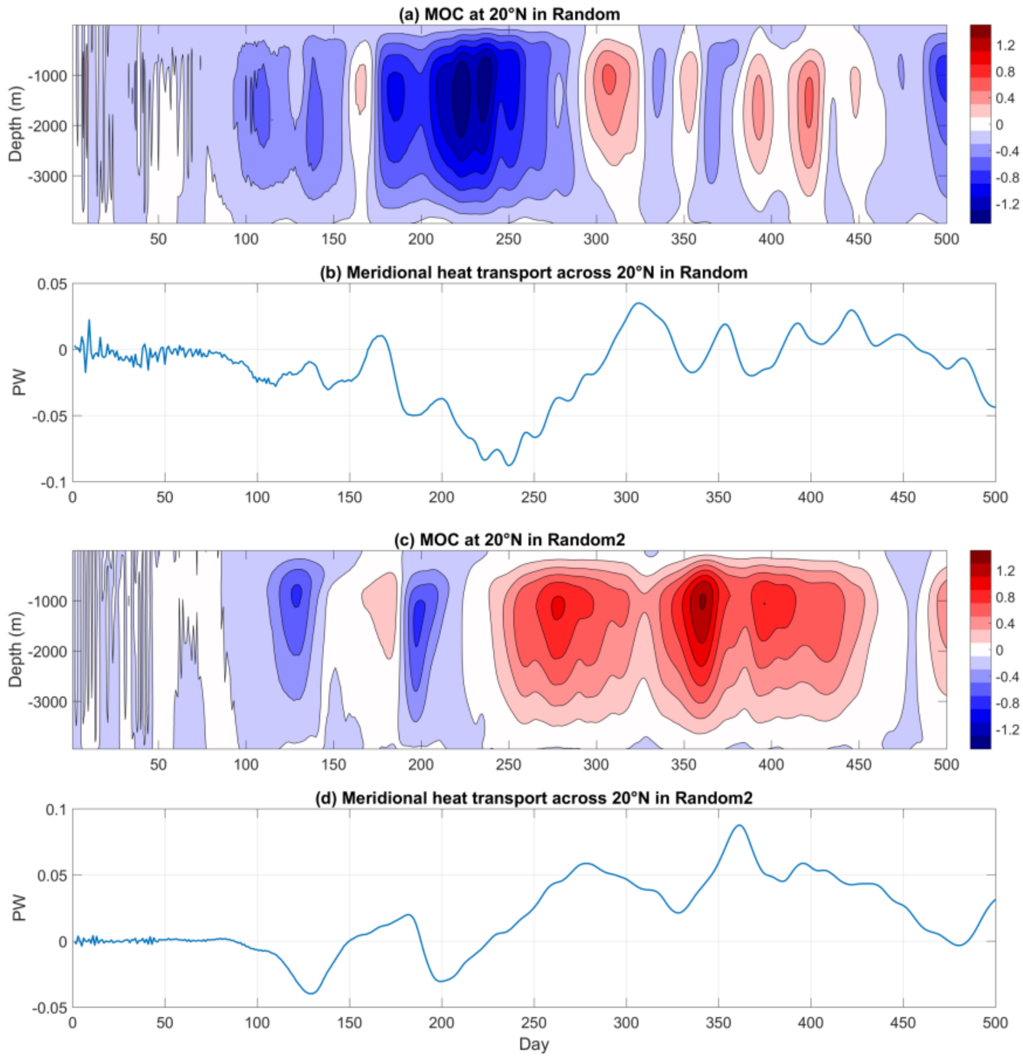

Figure 8: (a) Eddy-induced MOC (Sv) and (b) meridional heat transport (PW) at 20°N in Random experiment. (c) and (d) are the same as (a) and (b), but for Random2 experiment.

water, T is the potential temperature, and H_b is the depth of ocean bottom. The eddy-induced MOC anomalies are found to be deep-reaching, with peak values close to 1.5 Sv. Furthermore, these MOC anomalies are not short-lived but last for tens of days and sometime over one hundred days, for example, the negative MOC anomaly event on days 170-300 in Random. The eddy-induced meridional heat transport varies on the same time scales as the MOC anomalies, with each positive (negative) MOC anomaly event corresponding to a northward (southward) heat transport anomaly. The large negative MOC anomaly event on days 170-300 in Random results in an extended period of southward heat transport, with the peak magnitude approaching -0.1 PW. In Random2, a large positive eddy-induced MOC anomaly event is found to last for over 200 days, which yields an average northward heat transport anomaly of 0.05 PW over the 200-day period of this event. Comparisons between theoretically-predicted and model-simulated MOCs in Random and Random2 both show reasonable agreement. For example, the theory is able to capture the decline of the MOC in the first 200 days or so as well as its subsequent recovery in Random (Fig. 7b).

4.3. Atlantic

In the Atlantic experiments where realistic bathymetry and satellite-derived eddy SSH fields are used, pressure anomalies are generated as eddies impinge on the western continental slope, and they propagate equatorward in other forms of coastal trapped waves such as topographic Rossby waves (e.g. Hughes et al., 2019), rather than Kelvin waves as in Random experiment which has a flat bottom and vertical sidewalls. Associated with these pressure anomalies are equatorward-propagating MOC anomalies (Figs. 9-11).

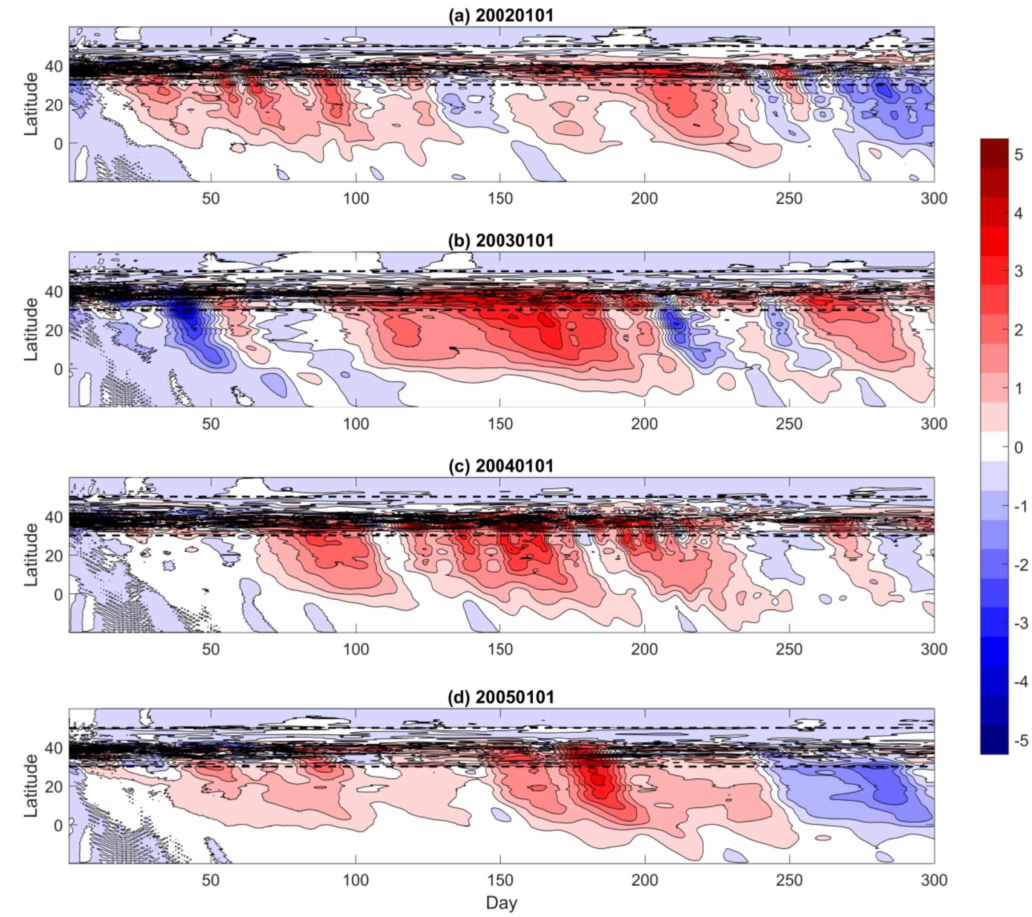

Figure 9: Hovmöller diagrams of MOC anomalies at 1500 m depth (Sv) in four Atlantic experiments initialised with satellite SSH fields in Januaries of 2002-2005. The dashed lines indicate the latitudinal limits of the initial eddy field.

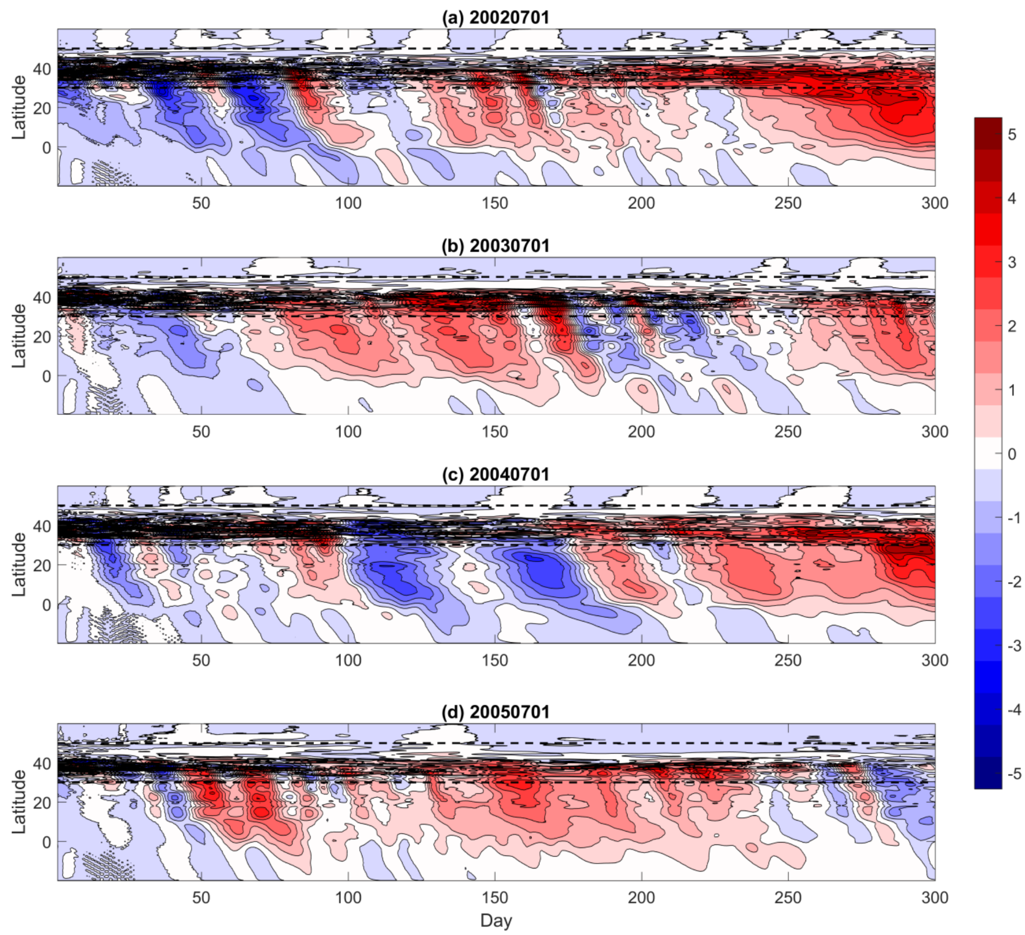

Figure 10: The same as Fig. 9, but for four Atlantic experiments initialised with satellite SSH fields in Julies of 2002-2005.

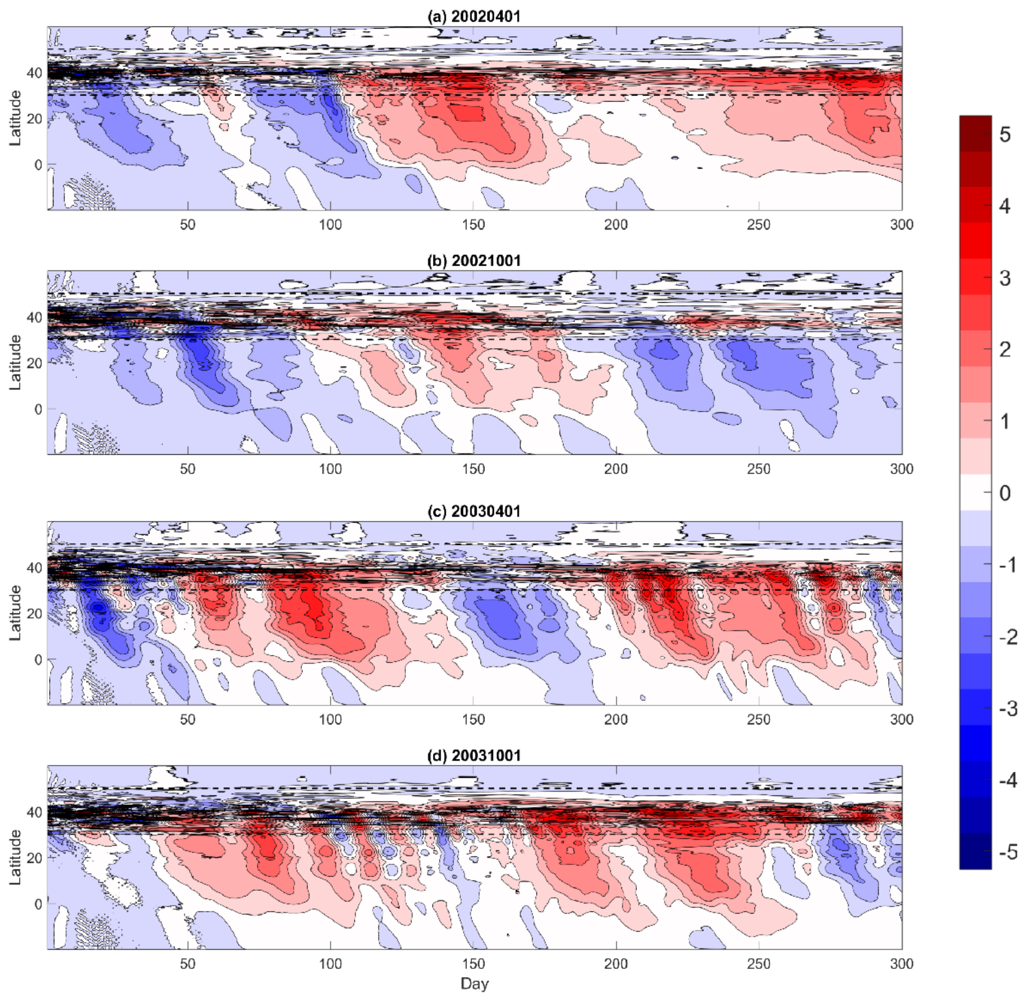

Figure 11: The same as Fig. 9, but for four Atlantic experiments initialised with satellite SSH fields in in Aprils and Octobers of 2002-2003.

There appear to be no systematic differences between experiments initialised in January and July in the four study years, or between these experiments and those initialised in April and October in year 2002 and 2003, i.e., no evidence suggesting a seasonal cycle of eddy-induced MOCs in the Atlantic experiments. In all twelve ensemble experiments, the MOC anomalies originate at the latitudes of the incident eddy band (30-50°N) and spread equatorward at speeds of approximately 2 to 3 m s^{-1}. The duration and magnitude of these MOC anomaly events are variable and irregular, ranging from less than 10 days to over 3 months and from less than 1 Sv to close to 5 Sv.

Figure 12 shows Hovmöller diagrams of MOC streamfunctions at 27°N from four Atlantic experiments initialised in Januaries and Julies of year 2002 and 2003, close to the latitude of the RAPID array. Results from experiments initialised in Aprils and Octobers of year 2002 and 2003 and those initialised in Januaries and Julies of year 2004 and 2005 are very similar (not shown). The eddy-induced MOC anomalies are again deep-reaching and significant, with some anomalies reaching a magnitude of over 5 Sv and lasting for longer than 100 days. In comparison, the Atlantic MOC estimated from the RAPID array has an average strength of 16.9 Sv and standard deviation of 4.4 Sv from April 2004 to October 2015 (e.g. Cunningham et al., 2007; McCarthy et al., 2012). These eddy-induced MOC anomalies lead to considerable meridional heat transport variability across 27°N, with values of $\mathcal{H}$ frequently exceeding ± 0.1 PW (Fig. 13). For example, there is a significant positive MOC anomaly event on days 100-200 in the experiment initialised with satellite SSH field on January 1st, 2003 (Fig. 12b), which leads to northward heat transport of $\mathcal{H} > 0.1$ PW during almost the whole

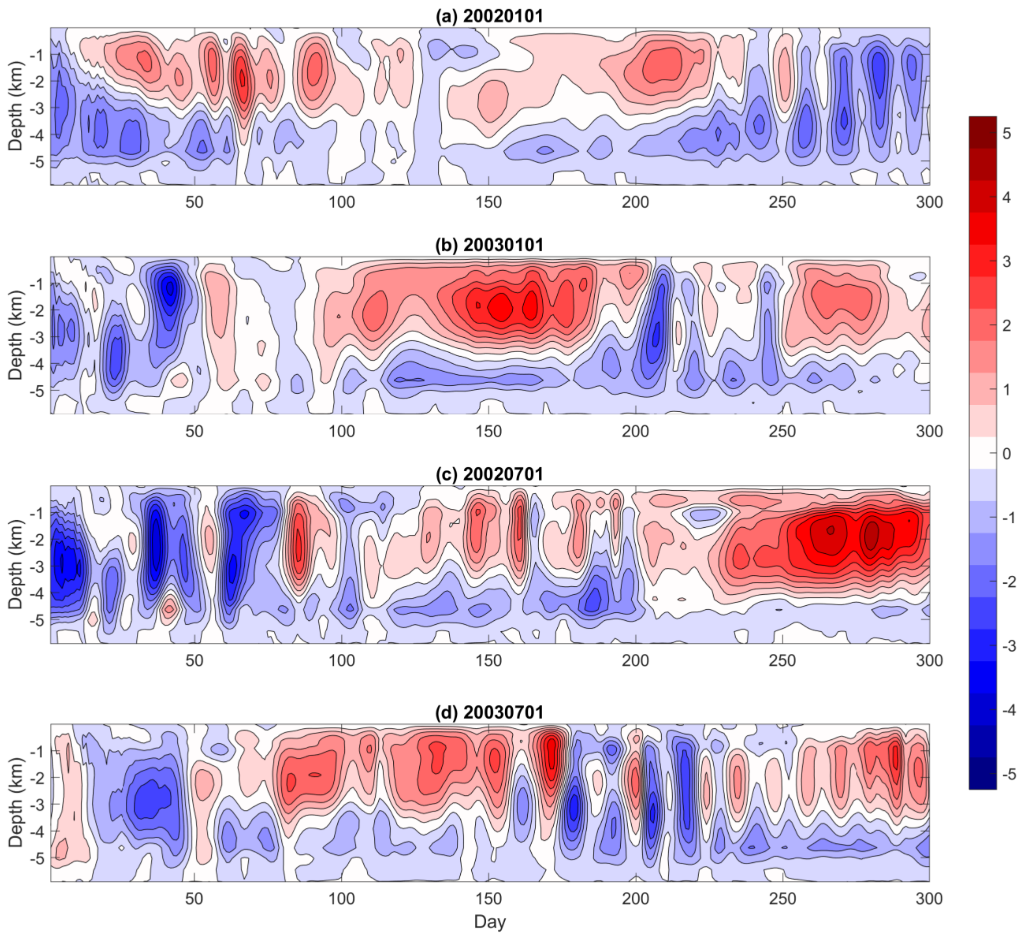

Figure 12: Eddy-induced MOC streamfunctions (Sv) at 27°N in four Atlantic experiments initialised with satellite SSH fields in Januaries and Julies of 2002-2003.

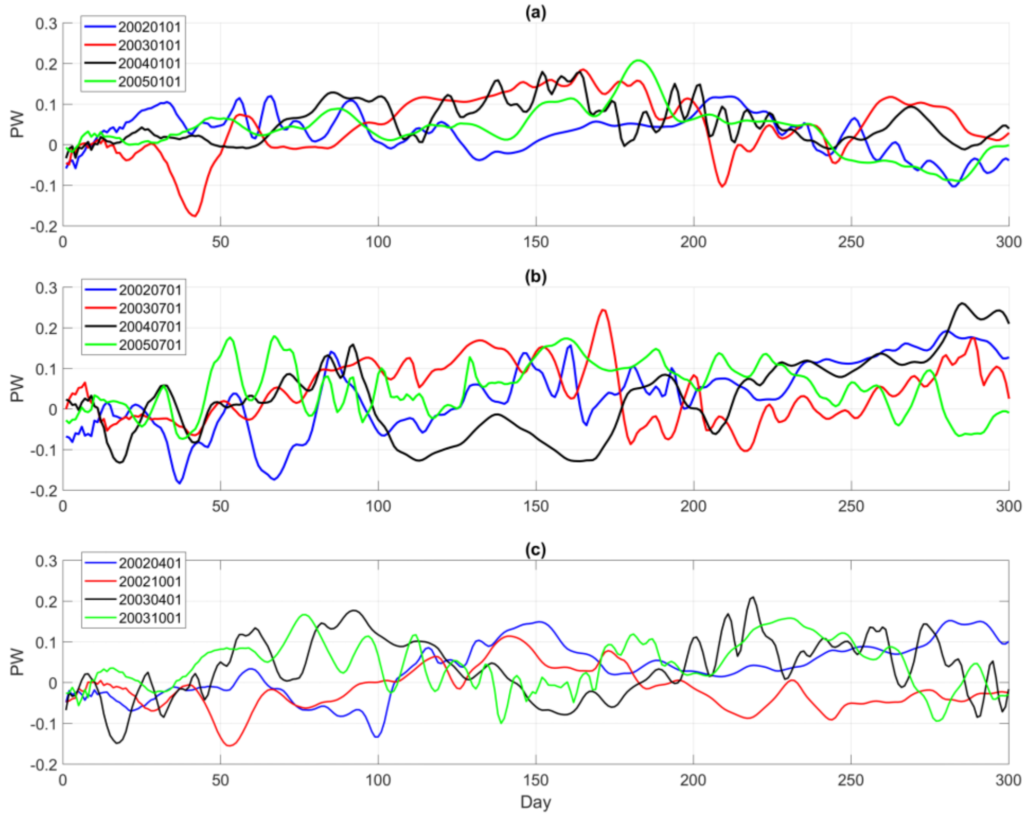

Figure 13: Eddy-induced meridional heat transport (PW) across 27°N in Atlantic experiments initialised with satellite SSH fields in (a) Januaries of 2002-2005, (b) Julies of 2002-2005 and (c) Aprils and Octobers of 2002-2003.

100 day period of this event (red curve in Fig. 13a). Recall that meridional heat transport in the North Atlantic achieved by the time-mean MOC driven by large-scale wind stress and buoyancy forcing is approximately 1 PW. These results therefore highlight the importance of MOC variability induced by westward-propagating eddies impinging on the western boundary.

5. Conclusions

Ocean eddies are observed to propagate ubiquitously westward, apart from in the Antarctic Circumpolar Current and separated western boundary currents. While the eddy energy is dissipated in the western boundary "graveyard" (Zhai et al., 2010; Yang et al., 2021), what happens to volume anomalies carried westward by the eddies remains unclear. In this study we have investigated meridional transport variability induced by westward-propagating eddies impinging on the western boundary. A simple quantitative theory has been developed in the framework of the reduced-gravity model. The theory predicts that the eddy-induced meridional transport at latitudes equatorward of an incident eddy field depends on eddy thickness anomalies propagated into the western boundary by long Rossy waves integrated over the latitude range of the whole eddy field. Therefore, when eddies of the same polarity simultaneously arrive at the western boundary, they are able to generate particularly large meridional transport anomalies. There are, however, limitations associated with our simple reduced-gravity model approach. For example, there is no mean flow advection and the model assumes vertical sidewalls. In deriving the theory, we have also assumed that the western boundary layer is narrow such that the time delay caused by eddy thickness anomalies crossing the narrow western boundary layer can be neglected. One way to account for this time delay is to include a time lag in (5), i.e.,

$$T_s(t) = -\int_{y_s}^{y_n} \frac{\beta g' H}{f^2} h_b \left(y, t - \frac{x_b - x_w}{c(y)} \right) dy, \tag{15}$$

where $(x_b - x_w)/c(y)$ is the time it takes for long Rossby waves to cross the western boundary region. For the single eddy experiments, $c \approx 4.5$ cm s^{-1}

and $x_b - x_w \approx 80$ km, which gives a time lag of ∼20 days, comparable to the lag between the model-simulated and theoretically-predicted MOC anomalies shown in Fig. 7a.

We then carry out a suite of numerical experiments using the MITgcm to examine eddy-induced meridional transport variability, ranging from a simple Gaussian eddy interacting with vertical western sidewall to satellite-derived ocean eddy field interacting with realistic western boundary geometry. Results from these experiments show that eddies impinging on the western boundary excite boundary trapped waves that propagate equatorward along the western boundary, and this leads to meridionally coherent MOC anomalies at latitudes equatorward of the incident eddy field. There are reasonable agreements between MOC anomalies predicted by the theory and those simulated by the model. The eddy-induced MOC anomalies are found to be deep-reaching and significant, with some anomalies reaching a magnitude of over 5 Sv and lasting longer than 100 days, particularly in the Atlantic experiments where realistic bathymetry and satellite-derived eddy SSH fields are used. Our results suggest that part of the MOC variability seen in the RAPID array observations is eddy-driven and as such is stochastic in nature. Furthermore, these eddy-induced MOC anomalies lead to considerable meridional heat transport variability. During large MOC anomaly events, the associated meridional heat transport anomalies often exceed ±0.1 PW during the whole period of the events (sometimes over 100 days). Such large and sustained meridional heat transport anomalies are expected to cause changes in ocean heat content and sea surface temperature, with implications for seasonal and interannual climate variability and prediction (e.g. Goddard et al., 2001; Bryden et al., 2014). The importance of eddy-induced stochastic MOC variability poses challenges to the development of future eddy parameterisation schemes for use in coarse-resolution ocean climate models that do not explicitly resolve mesoscale ocean eddies (e.g. Marshall et al., 2012; Porta Mana and Zanna, 2014; Jansen and Held, 2014).

Acknowledgements

XZ acknowledges support by a Royal Society International Exchanges Award (IEC/NSFC/170007) and partial support from the U.K. Natural Environmental Research Council (NE/R000999/1). ZY is supported by a scholarship from the Chinese Scholarship Council and the National Natural Science Foundation of China (41776006). We thank the two anonymous reviewers for their insightful and constructive comments that led to significant improvement of this manuscript.

References

Biastoch, A., Böning, C. W., Getzlaff, J., Molines, J. M., Madec, G., 2008. Causes of inter annual-decadal variability in the meridional overturning circulation for the midlatitude North Atlantic Ocean. J. Climate 21, 6599–6615.

Brannigan, L., Marshall, D. P., Garabato, A. C. N., Nurser, A. J. G., 2015. The seasonal cycle of submesoscale flows. Ocean Modell. 92, 69–84.

Bryden, H. L., King, B. A., McCarthy, G. D., McDonagh, E. L., 2014. Impact of a 30% reduction in Atlantic meridional overturning during 2009-2010. Ocean Sci. 10, 683–691.

Cessi, P., Louazel, S., 2001. Decadal oceanic response to stochastic wind forcing. J. Phys. Oceanogr. 31, 3020–3029.

Chelton, D. B., Schlax, M. G., Samelson, R. M., 2007. Global observations of large oceanic eddies. Geophys. Res. Lett. 34.

Chelton, D. B., Schlax, M. G., Samelson, R. M., 2011. Global observations of nonlinear mesoscale eddies. Prog. Oceanogr.

Cunningham, S. A., Kanzow, T., Rayner, D., Baringer, M. O., Johns, W. E., Marotzke, J., Longworth, H. R., Grant, E. M., Hirschi, J.-M., Beal, L. M., Meinen, C. S., Bryden, H. L., 2007. Temporal variability of the Atlantic meridional overturning circulation at 26.5^oN. Science 317, 935–938.

Domingues, R. M., Johns, W. E., Meinen, C. S., 2019. Mechanisms of eddy-driven variability of the Florida Current. J. Phys. Oceanogr. 49, 1319–1338.

Eden, C., Willebrand, J., 2001. Mechanism of interannual to decadal variability of the North Atlantic circulation. J. Climate 14, 2266–2280.

Ferrari, R., Wunsch, C., 2009. Ocean circulation kinetic energy: reservoirs, sources, and sinks. Annu. Rev. Fluid Mech. 41, 253–282.

Frolov, S. A., Sutyrin, G. G., Rowe, G. D., Rothstein, L. M., 2004. Loop current eddy interaction with the western boundary in the Gulf of Mexico. J. Phys. Oceanogr. 34, 2223–2237.

Goddard, L., Mason, S., Zebiak, S., Ropelewski, C., Basher, R., Cane, M., 2001. Current approaches to seasonal to interannual climate predictions. Int. J. Climatol. 21, 1111–1152.

Godfrey, J., 1975. On ocean spindown I: A linear experiment. J. Phys. Oceanogr. 5, 399–409.

Hughes, C. W., Fukumori, I., Griffies, S. M., Huthnance, J. M., Minobe, S., Spence, P., Thompson, K. R., Wise, A., 2019. Sea level and the role of coastal trapped waves in mediating the influence of the open ocean on the coast. Surv. Geophys. 40, 1467–1492.

Jansen, M. F., Held, I. M., 2014. Parameterization subgrid-scale eddy effects using energetically consistent backscatter. Ocean Modell. 80, 36–48.

Jayne, S. R., Marotzke, J., 2001. The dynamics of ocean heat transport variability. Rev. Geophys. 39, 385–411.

Johnson, H. L., Marshall, D. P., 2002. A theory for the surface Atlantic response to thermohaline variability. J. Phys. Oceanogr. 32, 1121–1132.

Mahajan, S., Zhang, R., Delworth, T. L., 2011. Impact of the Atlantic Meridional Overturning Circulation (AMOC) on Arctic surface air temperature and sea-ice variability. J. Clim. 24, 6573–6581.

Marshall, D. P., Johnson, H. L., 2013. Propagation of meridional circulation anomalies along western and eastern boundaries. J. Phys. Oceanogr. 43, 2699–2717.

Marshall, D. P., Maddison, J. R., Berloff, P. S., 2012. A framework for parameterizing eddy potential vorticity fluxes. J. Phys. Oceanogr. 42, 539–557.

Marshall, D. P., Vogel, B., Zhai, X., 2013. Rossby rip currents. Geophys. Res. Lett. 40, 4333–4337.

Marshall, J., Adcroft, A., Hill, C., Perelman, L., Heisey, C., 1997. A finite-volume, incompressible Navier Stokes model for studies of the ocean on parallel computers. J. Geophys. Res. 102, 5753–5766.

McCarthy, G., Frajka-Williams, E., Johns, W. E., Baringer, M. O., Meinen, C. S., Bryden, H. L., Rayner, D., Duchez, A., Roberts, C., Cunningham, S. A., 2012. Observed interannual variability of the atlantic meridional overturning circulation at 26.5^{o}N. Geophys. Res. Lett. 39.

Minobe, S., Terada, M., Qiu, B., Schneider, N., 2017. Western boundary sea level: A theory, rule of thumb, and application to climate models. J. Phys. Oceanogr. 47, 957–977.

Ni, Q., Zhai, X., Wang, G., Marshall, D. P., 2020. Random movement of mesoscale eddies in the global ocean. J. Phys. Oceanogr. 50, 2341–2357.

Porta Mana, P. G. L., Zanna, L., 2014. Toward a stochastic parameterization of ocean mesoscale eddies. Ocean Modell. 79, 1–20.

Shi, C., Nof, D., 1994. The destruction of lenses and generation of wodons. J. Phys. Oceanogr. 24, 1120–1136.

Smith, D., 1986. A numerical study of Loop Current eddy interaction with topography in the western Gulf of Mexico. J. Phys. Oceanogr. 16, 1260–1272.

Smith, D., O'Brien, J., 1983. The interaction of a two-layer isolated mesoscale eddy with bottom topography. J. Phys. Oceanogr. 13, 1681–1697.

Sutyrin, G. G., Rowe, G. D., Rothstein, L. M., Ginis, I., 2003. Baroclinic eddy interactions with continental slopes and shelves. J. Phys. Oceanogr. 33, 283–291.

Thomas, M. D., Zhai, X., 2013. Eddy-induced variability of the meridional overturning circulation in a model of the North Atlantic. Geophys. Res. Lett. 40, 2742–2747.

Vellinga, M., Wood, R. A., 2002. Global climatic impacts of a collapse of the Atlantic thermohaline circulation. Clim. Change 54, 251–267.

Vic, C., Roullet, G., Capet, X., Carton, X., Molemaker, M. J., Gula, J., 2015. Eddy-topography interactions and the fate of the Persian Gulf Outflow. J. Geophys. Res. 120, 6700–6717.

Wei, J., Wang, D. P., 2009. A three-dimensional model study of warm core ring interaction with continental shelf and slope. Cont. Shelf Res. 29, 1635–1642.

Wise, A., Hughes, C. W., Polton, J. A., 2018. Bathymetric influence on the coastal sea level response to ocean gyres at western boundaries. J. Phys. Oceanogr. 48, 2949–2964.

Yang, Z., Zhai, X., Marshall, D. P., Wang, G., 2021. An idealized model study of eddy energetics in the western boundary ’graveyard’. J. Phys. Oceanogr. 51, 1265–1282.

Zhai, X., Johnson, H. L., Marshall, D. P., 2010. Significant sink of ocean-eddy energy near western boundaries. Nature Geoscience 3, 608–612.

Zhai, X., Johnson, H. L., Marshall, D. P., 2014. A simple model of the response of the Atlantic to the North Atlantic Oscillation. J. Clim. 27, 4052–4069.

Zhang, Z., Zhang, Y., Wang, W., Huang, R. X., 2013. Universal structure of mesoscale eddies in the ocean. Geophys. Res. Lett. 40, 3677–3681.